PNAS
www.pnas.org

Supplementary Information for

Unveiling the High Activity Origin of Single Atom Iron Catalysts for Oxygen Reduction Reaction

Liu Yang[#], Daojian Cheng[#], Haoxiang Xu, Xiaofei Zeng, Xin Wan, Jianglan Shui, Zhonghua Xiang, Dapeng Cao*

Corresponding Author: Dapeng Cao
[*] Email: caodp@mail.buct.edu.cn
[#] Equally contributed to this work

This PDF file includes:

www.pnas.org/cgi/doi/10.1073/pnas.1800771115

Supplementary Information Texts

Materials and Methods

Chemicals. Urea (95%, Alfar Aesar), Polyether F127 (98%, Alfar Aesar), $FeCl_3$ $6H_2O$ (Alfar Aesar) and HCl were purchased from Beijing Chemical Works. All chemicals used in the synthesis of self-designed catalysts are analytical regents (AR).

Synthesis of electrocatalysts. 0.3 g g-C_3N_4 was dissolved in 50 ml deionized water, sonicated 1h to make it completely dissolved. Then 0.6g F127 was added into above solution, sonicated 2h and stirred 2h to make the F127 intact wrapped in g-C_3N_4. Then 0.5ml (0.3M $FeCl_3$ $6H_2O$) was injected into above solution. The well dispersed solution continued to stir 12h, then the solution was evaporated at 80℃. The dried sample was carbonized at 550℃ for 2h with the heating rate 3℃/min and then continue to heat to 800℃ for 2h with the heating rate 3 ℃/min in a N_2 atmosphere. The carbonized product was etched by 2 M hydrochloric acid for 24 h at room temperature, and then the SA-Fe/NG catalyst was obtained, which was labeled as SA-Fe/NG catalyst. Similarly, Fe/NG was obtained by above procedures but without the addition of F127.

Characterizations. The scanning electron microscope (SEM) images of the samples were obtained by HITACHI S-4800. TEM images were received by a TECNAI G2 F20 field emission transmission electron microscope at 200 kV. The morphologies of the catalysts were further characterized by aberration-corrected scanning transmission electron microscopy (ACSTEM) equipped with an electron energy loss spectrometer (EELS) onJEM-ARM200F. Powder X-ray diffraction (PXRD) were obtained by a D8 ADVANCE X-ray diffract meter (Cu Kα radiation 40 kV, 20 mA, λ =1.54178 Å). High-resolution TEM (HRTEM) was carried out using an image spherical aberration–corrected TEM system (FEI Titan 80-300) with an acceleration voltage of 80 kV. N_2 adsorption/desorption isotherm 77 K was measured by an ASAP 2460 analyzer (Micromeritics, U.S.A). The specific surface area (S_{BET}) was calculated by the Brunauer-Emmet-Teller (BET) method and the pore size distribution was evaluated by non-local density functional theory (NLDFT). X-ray photoelectron spectroscopy (XPS) measurements were carried out by a Thermo Fisher ESCALAB 250 X-ray photoelectron spectrometer equipped with an A1 Kα X-ray source. X-ray Absorption Fine Structure (XAFS) was performed at the beam line 4W1B of Beijing Synchrotron Radiation Facility (BSRF), in China. The storage rings of BSRF were operated at 2.5 GeV with a maximum current of 250 mA. EXAFS data were collected using a fixed-exit double-crystal Si (111) monochromator. Fe Kedge EXAFS data were analyzed using standard procedures with the program IFEFFIT. Mössbauer spectrum was recorded in transmission mode with a ^{57}Co source in a rhodium matrix. The absorber and operated source in Mössbauer spectrometer of the electromechanical type were fixed on constant acceleration mode, which was calibrated by using an α-Fe foil.

Electrochemical Measurements. All the electrochemical measurements were performed in a general three-electrode system on an electrochemical workstation (CHI760e, Shanghai Chenhua Instrument Factory, China), in which saturated calomel electrode (SCE) regarded as a reference electrode, 1 cm^2 platinum net as the counter electrode and 0.1M KOH or 0.5 M H_2SO_4 or 0.1 M $HClO_4$aqueous solution as electrolyte. RHE calibration was performed in the high purity hydrogen saturated alkaline and acidic solutions with a Pt foil as the working electrode and a Pt wire as the counter electrode, as depicted in Figs S32 and S33. A rotating disk electrode and rotating ring-disk electrode were served as the substrate for the working electrodes. The electrolyte was saturated with oxygen by bubbling O_2 before the measurement. RDE measurements were conducted at a rate of 5 mV/s with different rotating speeds from 400 to 2025 rpm. RDE and RRDE tests were both detected by American Pine Instruments device.

For each sample (including SA-Fe/NG, Fe/NG, 20 wt% Pt/C), 5 mg synthesized carbon powder was dispersed in 0.2 mL ethanol and 0.8 mL deionized water, then added into 50 μL Nafion solution (5 wt %). The inks were sonicated for at least 0.5 h to obtain the homogeneous dispersion. The SA-Fe/NG, Fe/NG dispersed solutions were dropped on the glassy carbon electrode disk with loading of 10μL (~ 0.24 mg cm^{-2}) in 0.1M KOH aq and with 25μL (~ 0.6 mg cm^{-2}) in 0.5 M H_2SO_4 aq. The 20% Pt/C dispersed solution with loading 10μL (~48 μg cm^{-2}) regardless in 0.1M KOH or 0.1 M $HClO_4$ aq.

The RRDE examinations were carried out with the Pt ring electrode (the potential of the Pt ring was set at V = 1.3 V_{RHE}) to test the ring current (I_{ring}). The polarization curves were examined at a disk rotation rate of 1600 rpm. The peroxide yield (HO_2^- %) and the electron transfer number (n) were calculated by

$$n = 4 \times \frac{I_{disk}}{\left(\frac{I_{ring}}{N}\right) + I_{disk}}$$

$$H_2O_2(\%) = 200 \times \frac{I_{ring}}{\left(\frac{I_{ring}}{N}\right) + I_{disk}}$$

I_{disk} is the disk current, and I_{ring} is the ring current. N is the current collection efficiency of the Pt ring that is 0.42.

The polarization curves were collected at disk rotation rates of 400, 625, 900, 1225, 1600 and 2025 rpm for the RDE examination. For calculating the number of electrons transferred (n), we utilized Koutecky–Levich equations to analyze the kinetic parameters on the basis of the:

$$\frac{1}{J} = \frac{1}{J_L} + \frac{1}{J_K} = \frac{1}{J_K} + \frac{1}{B\omega^{1/2}}$$

$$B = 0.62nFC_0D^{2/3}\upsilon^{-1/6}$$

$$J_K = \frac{J \times J_L}{J_L - J}$$

where J is the measured current density, J_k, J_L are the kinetic- limiting current densities and diffusion-limiting current densities, respectively. is the angular velocity. F is the Faraday constant (F 96500 C/mol). C_0 is the bulk concentration of O_2 in 0.1 M KOH (mol/cm^3). D is the diffusion coefficient of O_2 in alkaline and acidic solution cm^2/s). υ is the kinematic viscosity of the electrolyte (0.01 cm^2/s) and k is the electron-transfer rate constant.

PEMFC tests. The catalyst was mixed with Nafion® alcohol solution (5 wt%, Aldrich), isopropanol and deionized water to prepare the catalyst ink, which contained the same weight of Nafion ionomer as the catalyst. The ink was subjected to a sonication and stirring. The well-dispersed ink was brushed on a piece of carbon paper (5 cm^2), followed by a drying in vacuum at 80 ℃ for 2 h. The prepared cathode and anode were pressed onto the two sides of a Nafion 211 membrane (DuPont) at 130 ℃ for 90 seconds under a pressure of 1.5 MPa to obtain the membrane electrode assembly (MEA). Polarization plots were recorded using fuel cell test station (Scribner 850e) in a current-scanning mode. UHP-grade H_2 and O_2 humidified at 80 ℃ were supplied to the anode and cathode at a flow rate of 0.3 and 0.4 L min^{-1}, respectively. The cell temperature was maintained at 80 ℃. The backpressures at both electrodes were set at 2.0 bar. After recording the polarization curves, a 20-h stability test was performed on the same MEA, while the flow rates of the gas was switched to 0.1 L min^{-1} for both electrodes.

Zn-air battery. We assembled a home-made Zn-air battery, in which 6 M KOH with 0.2 M ZnO was employed as electrolyte, and a zinc piece and SA-Fe/NG -loaded carbon paper (1 mg/cm^2) served as the anode and air cathode, respectively. The stability of SA-Fe/NG was evaluated by a rechargeable Zn-air battery, the measurements run 30 cycles, 40 min for a charging and discharging cycle. The mass loading of SA-Fe/NG and 20%Ir/C is 1 mg/cm^2 for rechargeable air electrode, respectively.

Computational details: Geometry optimization and total energy calculations were performed by using first-principle calculations within the framework of density functional theory (DFT), as implemented in the plane wave set Vienna abinitio Simulation Package (VASP) code (1, 2) The Perdew-Burke-Ernzerhof (PBE) functional (3) within the generalized gradient approximation (GGA) was used to model the exchange correlation energy. The projector augmented wave (PAW) pseudo-potentials (4) were used to describe the interaction valence electron and ionic cores. The kinetic energy cut off of 500 eV was chosen for the plane-wave expansion to ensure that the energies were converged within 1 meV/per atom. A gaussian smearing with σ= 0.05 eV to the orbital occupation is applied to broaden the Fermi level for accurate electronic convergence, whilst a tetrahedron method with Blöchl corrections was employed for the accurate electronic structure calculations. Self-consistent-field (SCF) calculations were performed with an electronic structure iteration of 1×10^{-4} eV on the total energy. Geometry optimizations were performed by using the BFGS algorithm until the maximum force component of the system converges to 0.02 eV/Å.

Computational models: As shown in Fig. S26, two kinds of periodic rectangular unit cells with one Fe-N_4 active center per unit were used. A large vacuum slab of 15 Å was inserted in z direction for surface isolation to prevent interaction between two neighboring surfaces. The k-point sampling of the Brillioun zone was obtained using a $6\times7\times1$ grid for Fe@pyridinic N and $6\times6\times1$ grid for Fe@pyrrolic N by Monkhorst Pack Scheme. Denser k-points ($12\times14\times1$ and $12\times12\times1$) were used for the electronic structure calculations.

Reaction mechanism: The ORR activities on active sites of various electrocatalysts were studied in details according to the electrochemical framework developed by Nørskov and his co-workers (5). As for ORR, O_2 is reduced either through a two-electron process, or completely via a direct four-electron pathway. In an alkaline electrolyte (pH=14), H_2O rather than H_3O^+ may act as the proton donor, so the overall reaction scheme of the four-electron transfer ORR can be written as:

$$O_2+2H_2O+4e^-\leftrightarrow4OH^-$$

The four-electron transfer ORR may proceed through two possible mechanisms: the associative pathway that involves protonation of O_2 or a direct O_2 dissociation pathway. The associative mechanism can be split into the following elementary steps which are usually employed to investigate the electrocatalysis of the ORR on various materials:

$$O_2(g) + H_2O(l) + e^- \rightarrow OOH^* + OH^- \quad (S1)$$
$$OOH^* + e^- \rightarrow O^* + OH^- \quad (S2)$$
$$O^* + H_2O\,(l) + e^- \rightarrow OH^* + OH^- \quad (S3)$$
$$OH^* + e^- \rightarrow OH^- + * \quad (S4)$$

where * stands for an active site on the catalytic surface, (l) and (g) refer to liquid and gas phases, respectively, and O*, OH* and OOH* are adsorbed intermediates.

The mechanism for four-electron transfer ORR via direct O_2 dissociation pathway starts with the following elementary steps:

$$O_2\,(g) \rightarrow O_2^* \rightarrow 2O^*$$
$$2O^* + 2H_2O\,(l) + 2e^- \rightarrow 2OH^* + 2OH^-$$
$$2OH^* + 2e^- \rightarrow OH^- + *$$

According to the preview first principles computational works, (6-8) O_2 dissociation hardly exists on graphitic nitrogen-doped graphene surface due to the extremely high barriers. Additionally, we have also examined the O_2 dissociation pathway on Fe@pyridinic N and Fe@pyrrolic N as shown in Fig. S25. The energy barriers for O_2 dissociation are all above 1 eV, indicating that the dissociative $4e^-$ pathway is not surmountable at room temperature. Hence, in this work only the associative $4e^-$ reduction pathway is considered.
In addition, the two-electron transfer ORR under alkaline condition is generally reported to proceed according to the following elementary steps:

$$O_2(g) + H_2O(l) + e^- \rightarrow OOH^* + OH^- \quad (S5)$$

$$OOH^* + e^- \rightarrow OOH^- \quad (S6)$$

Reaction free energy: For proton-transfer steps, reaction free energies are regarded as approximate values of activation barriers(9). This approximation may result in a slight overestimation of activity for a given proton-transfer elementary step, but can still qualitatively represent the right relative energetic ordering of the various proton-transfer elementary steps. Therefore, we took reactions (S1)-(S6) to derive the thermochemistry for ORR. The Gibbs reaction free energy of these electrochemical elementary steps involving electron/proton transfer was obtained by using density functional theory (DFT) calculations accompanied with computational normal hydrogen electrode (NHE) model developed by Nørskov and co-workers (5, 10, 11). In this model, the calculation of reaction free energy is performed by setting up NHE as the reference electrode, which allows us to replace chemical potential with that of half a hydrogen molecule at standard conditions (U = 0 V vs NHE, pH=0, p = 1 bar, T = 298 K).
In order to obtain the reaction free energy of each elementary step in ORR on different sites for various model electrocatalysts, we calculated the adsorption free energy of O*, OH* and OOH*. Since it is difficult to obtain the exact free energy of OOH, O, and OH radicals in the electrolyte solution, the adsorption free energies ΔG_{OOH^*}, ΔG_{O^*}, and ΔG_{OH^*}, are relative to the free energy of stoichiometrically appropriate amounts of H_2O (g) and H_2 (g) , defined as follows:

$$\Delta G_{O^*} = E_{O^*} + E_{H2} - E_{H2O} - E^* + \Delta ZPE - T\times\Delta S$$

$$\Delta G_{OH^*} = E_{OH^*} + 0.5\times E_{H2} - E_{H2O} + \Delta ZPE - T\times\Delta S$$

$$\Delta G_{OOH^*} = E_{OOH^*} + 1.5\times E_{H2} - 2\times E_{H2O} + \Delta ZPE - T\times\Delta S$$

where T is the temperature and ΔS is the entropy change. The vibrational frequencies of adsorbed species (O*, OH*, and OOH*) were calculated with the model electrocatalysts that remain fixed to obtain zero-point energy (ZPE). Entropy values of gaseous molecules are taken from the standard tables in the Physical Chemistry text book (12), while the entropies of intermediates adsorbed on clusters are negligible. The entropy and zero-point energy (ZPE) corrections in determining the adsorption free energy are summarized in the Table S6.
For each elementary step, the Gibbs reaction free energy ΔG is defined as the difference between free energies of the initial and final states, which is given by the expression:

$$\Delta G = \Delta E + \Delta ZPE - T\Delta S + \Delta G_U + \Delta G_{PH}$$

where ΔE is the reaction energy of reactant and product molecules adsorbed on catalyst surface, obtained from DFT calculations; ΔZPE and ΔS are the change in zero point energies and entropy due to the reaction, respectively. The bias effect on the free energy of each initial, intermediate and final state involving an electron in the electrode is taken into account by shifting the energy of the state by $\Delta G_U = -neU$, where U is the electrode applied potential relative to NHE as mentioned above, e is the elementary charge transferred and n is the number of proton–electron pairs transferred. The change of free energy owing to the effect of a pH different from 0 of the electrolytic solution is considered by the correction for H^+ ions concentration ($[H^+]$) dependence of the entropy, $\Delta G_{PH} = -k_B T \ln[H^+] = pH \times k_B T \ln 10$, where k_B is the Boltzmann constant and T is the temperature. Hence, the equilibrium potential U_0 for four-electron transfer ORR at pH = 14 was determined to be 0.402V vs NHE or 1.23V vs RHE according to Nernst equation ($E = E^0 - 0.0591pH$, $U^0_{RHE} = U^0_{NHE} + 0.828V = 0.402 + 0.828 = 1.23V$), where the reactant and product are at

the same energy level. As for two-electron transfer ORR, the equilibrium potential U^0 at pH = 14 was determined to be 0.695V vs RHE. Given that the high-spin ground state of the oxygen molecule is poorly described in DFT calculations, the free energy of the O_2 molecule was derived according to $G_{O2}(g) = 2G_{H2O}(l) - 2G_{H2} + 4 \times 1.23$ (eV). The free energy of OH- was derived as $G_{OH^-} = G_{H2O}(l) - G_{H^+}$, where $G_{H^+} = 1/2G_{H2} - k_B T \ln 10 \times pH$. The free energy for gas phase water is calculated at 0.035 bars because this is the equilibrium pressure in contact with liquid water at 298 K. The free energy of gas phase water at these conditions is equal to the free energy of liquid water.

The reaction free energy of S1−S4 for four-electron transfer ORR can be expressed with the adsorption free energy of various oxygenated species (see Table S7), gas phase H_2 and H_2O defined earlier, which are

$$\Delta G1 = \Delta G_{OOH^*} - 4.92 + eU + pH \times kBT\ln 10 \quad \text{(S1)}$$

$$\Delta G2 = \Delta G_{O^*} - \Delta G_{OOH^*} + eU + pH \times kBT\ln 10 \quad \text{(S2)}$$

$$\Delta G3 = \Delta G_{OH^*} - \Delta G_{O^*} + eU + pH \times kBT\ln 10 \quad \text{(S3)}$$

$$\Delta G4 = -\Delta G_{OH^*} + eU + pH \times kBT\ln 10 \quad \text{(S4)}$$

The reaction free energy of S5−S6 for two-electron transfer ORR can be calculated using the following equations:

$$\Delta G5 = \Delta G_{OOH^*} - 4.92 + eU + pH \times kBT\ln 10 \quad \text{(S5)}$$

$$\Delta G6 = 3.53 - \Delta G_{OOH^*} + eU + pH \times kBT\ln 10 \quad \text{(S6)}$$

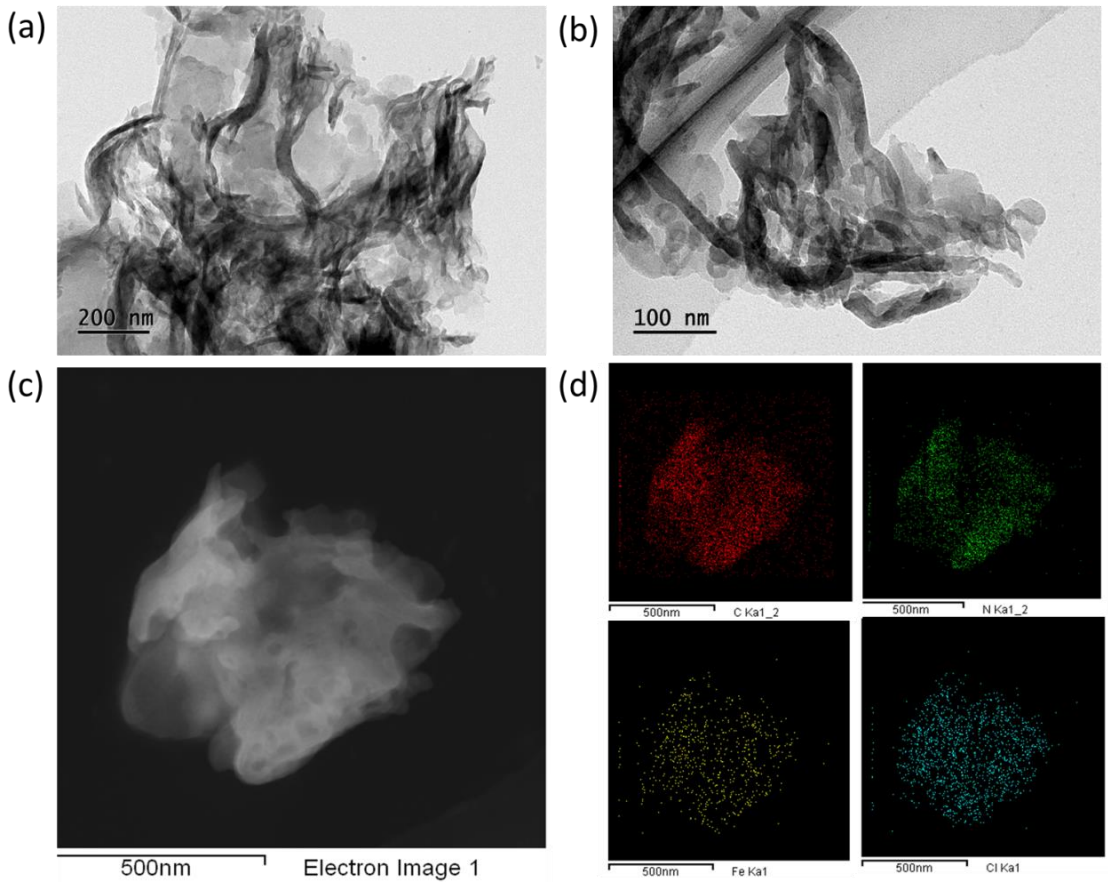

Fig. S1. (a) (b) The TEM image of precursor g-C_3N_4. (c) TEM image of precursor of g-C_3N_4/Fe. (d) The corresponding mappings of C, N, Fe and Cl elements distributed in the precursor of g-C_3N_4/Fe.

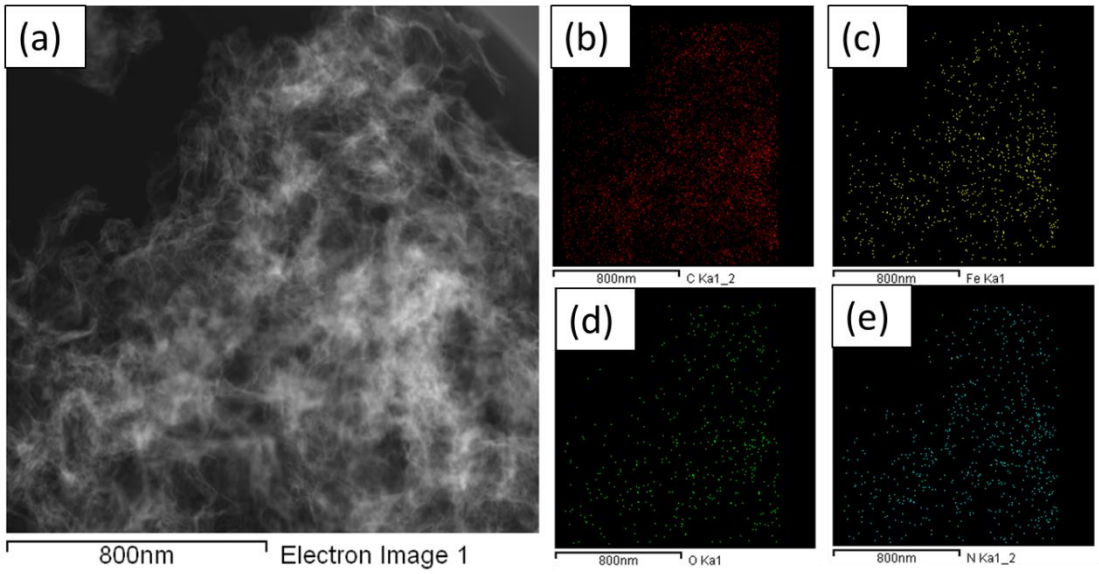

Fig. S2. (a) TEM image of SA-Fe/NG. (b-e) The corresponding mappings of C, Fe, O and N elements distributed in the SA-Fe/NG.

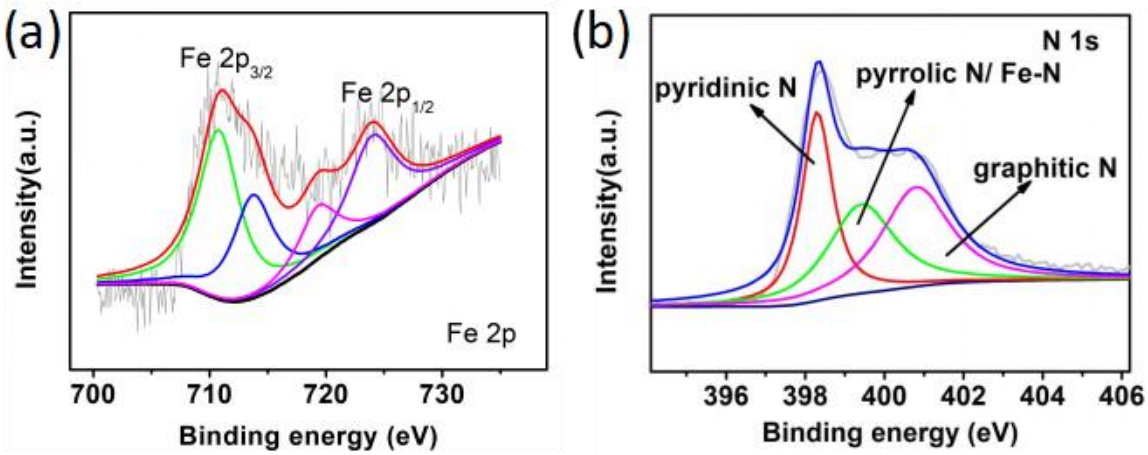

Fig. S3. High-resolution XPS spectra of (a) Fe 2p and (b) N 1s for SA-Fe/NG.

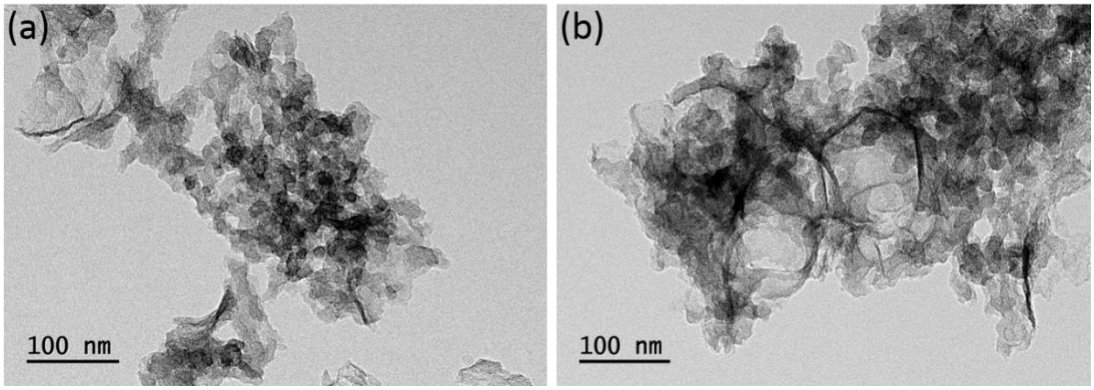

Fig. S4. (a) (b) The TEM image of Fe/NG.

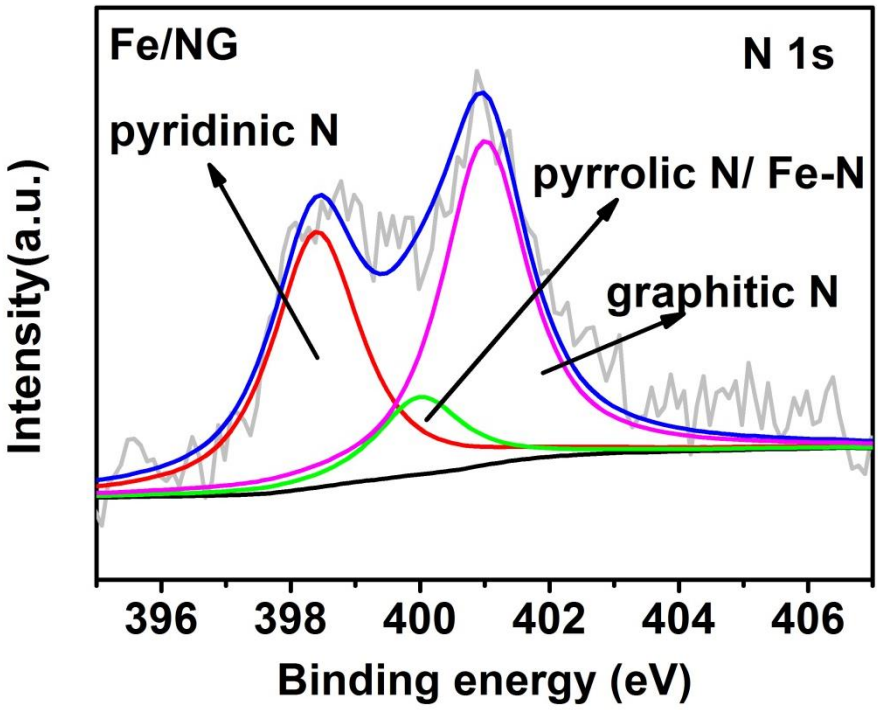

Fig. S5. High-resolution XPS spectra of N1s for Fe/NG.

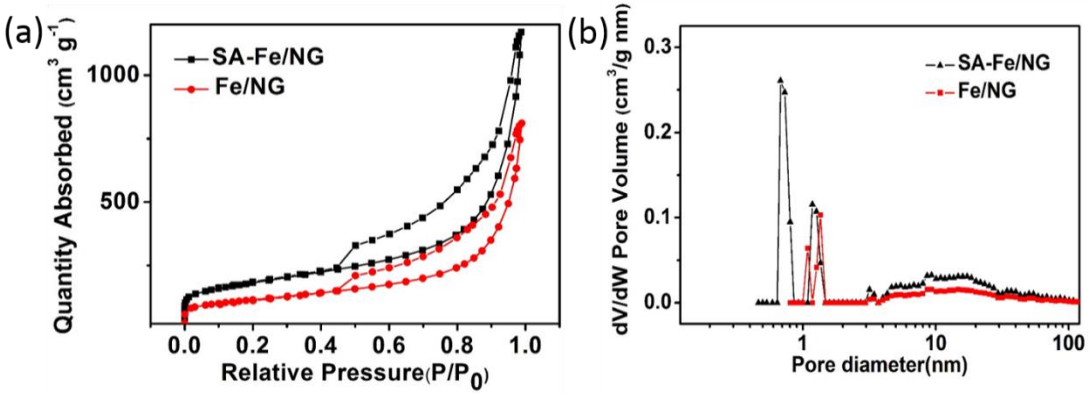

Fig. S6. (a) N_2 adsorption–desorption isotherms at T=77 K and (b) the pore size distributions of SA-Fe/NG and Fe/NG.

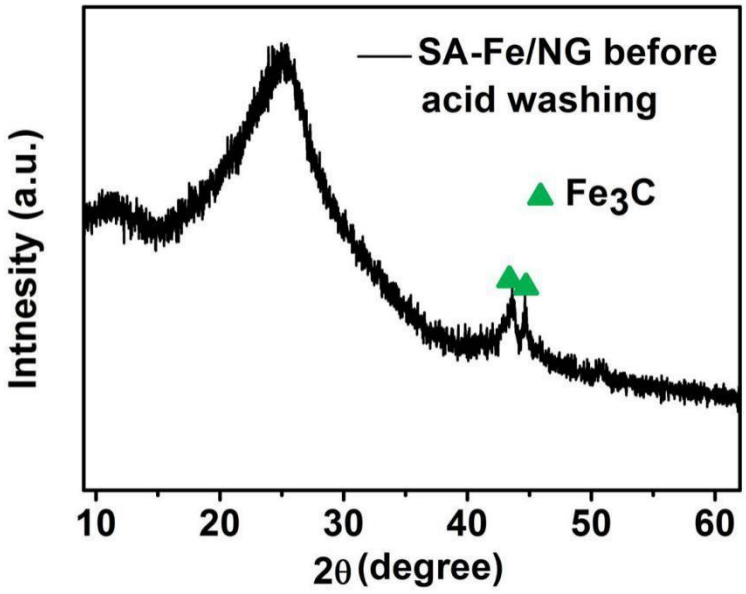

Fig. S7. PXRD graph of SA-Fe/NG before acid washing.

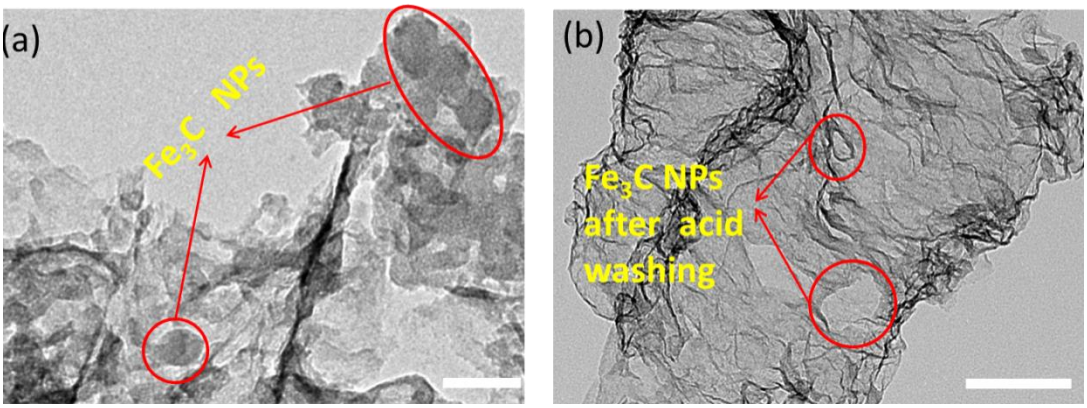

Fig. S8. The TEM image of SA-Fe/NG (a) before (scale bar, 100 nm) and (b) after acid washing (scale bar, 200 nm).

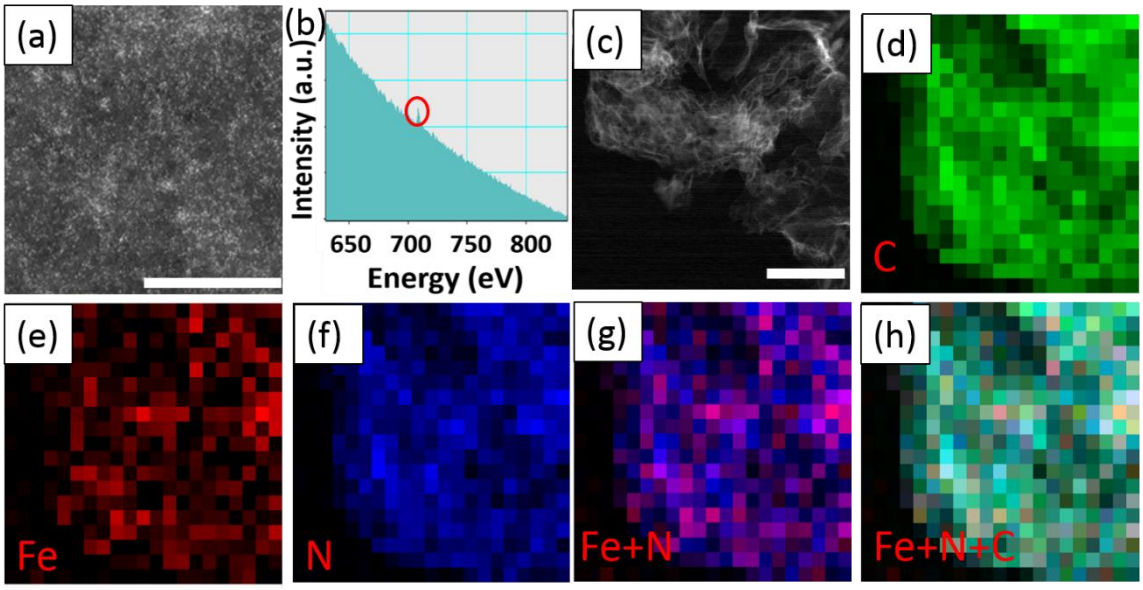

Fig. S9. (a) HAADF STEM image of the SA-Fe/NG with iron atom bright points (scale bar, 10 nm). (b) The electron energy loss spectroscopy (EELS) atomic spectra of Fe element from the bright points, where the Fe was signed by red circle (c) TEM image of SA-Fe/NG, scale bar, 200 nm. (d-h) EELS mapping of carbon, iron, nitrogen, and superimposed iron and nitrogen and superimposed iron, nitrogen and carbon for SA-Fe/NG.

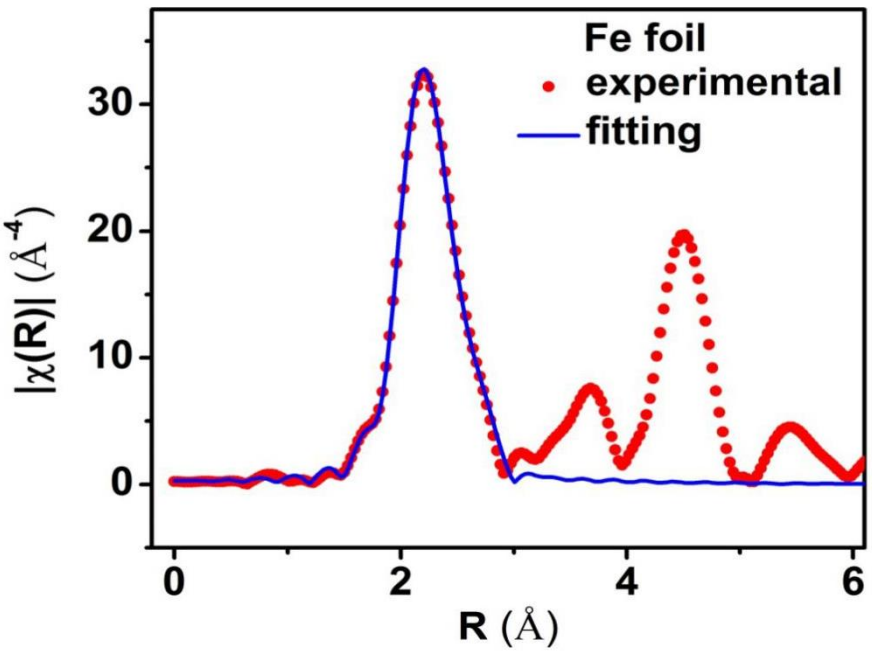

Fig. S10. Fourier-transformed of Fe K-edge spectra of Fe foil and corresponding fitting.

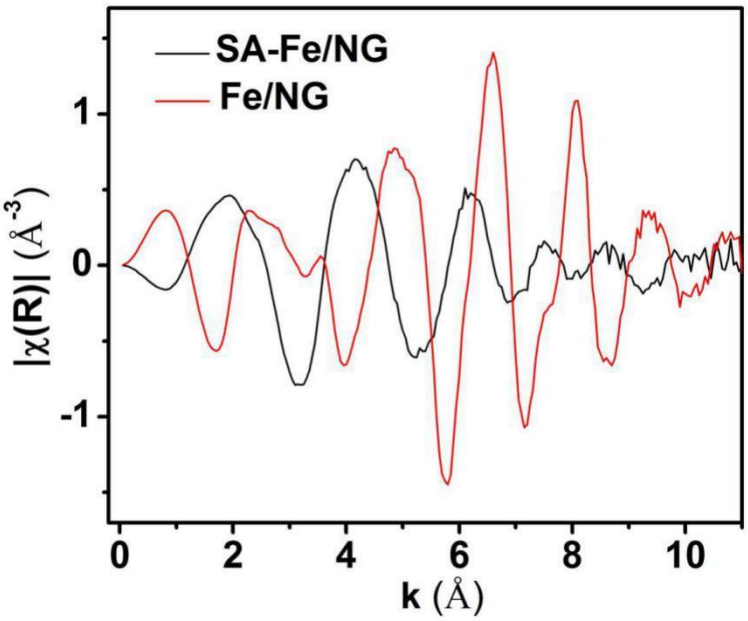

Fig. S11. The corresponding EXAFS k space curves of SA-Fe/NG and Fe/NG.

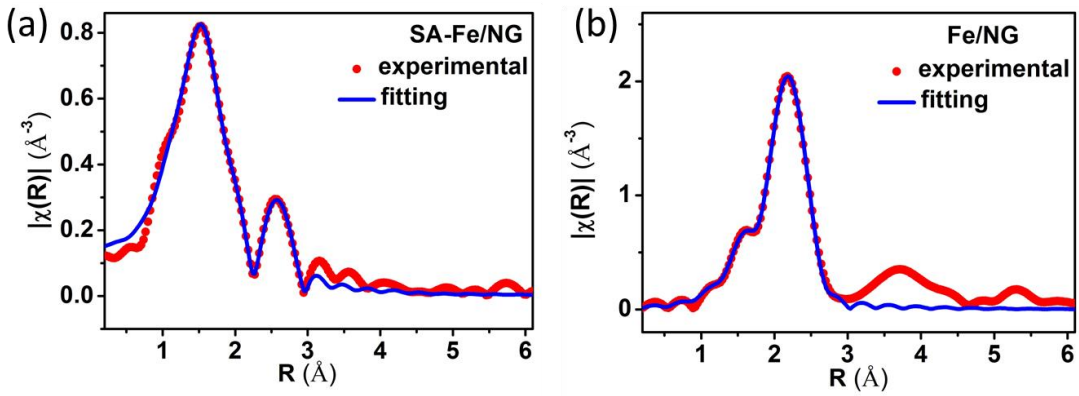

Fig. S12. Fourier-transformed of Fe K-edge spectra of (a) SA-Fe/NG and (b) Fe/NG and corresponding fitting.

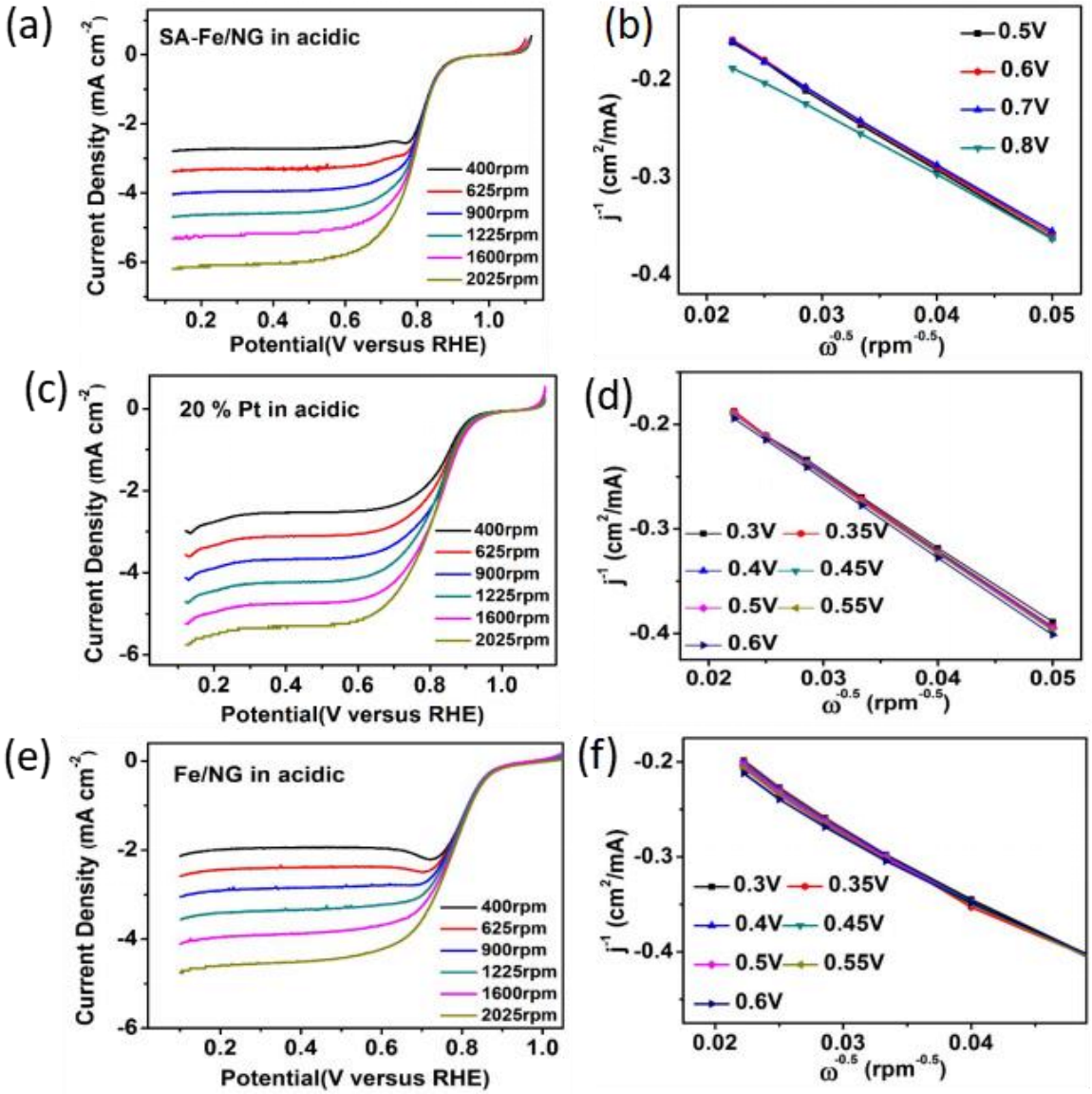

Fig. S13. RDE linear sweep voltammograms of SA-Fe/NG (a), and Fe/NG (e) at different rotating speeds in O_2-saturated 0.5 M H_2SO_4 solution and 20% Pt/C (c) in 0.1M $HClO_4$ with a sweep rate of 5 mV/s at the different rotating rates (400 rpm-2025 rpm). Corresponding Koutecky-Levich plots of SA-Fe/NG (b), 20% Pt/C (d), Fe/NG (f) derived from RDE at different potentials.

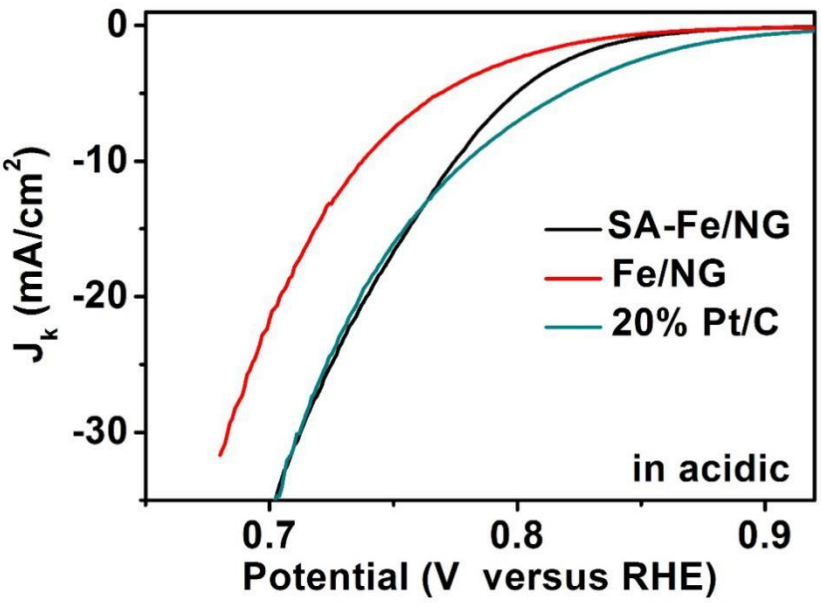

Fig. S14. Kinetic current density of SA-Fe/NG and Fe/NG in O_2-saturated 0.5M H_2SO_4, 20% Pt/C in 0.1 M $HClO_4$.

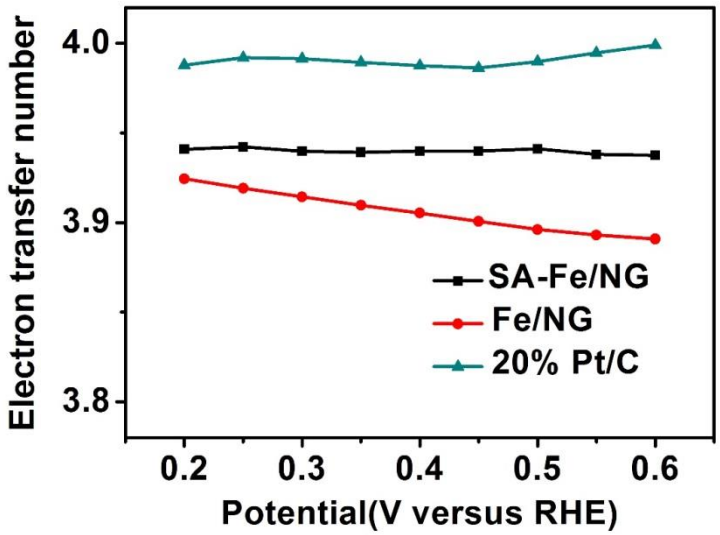

Fig. S15. The electron transfer number n at different potentials (0.2 V- 0.6 V) in O_2-saturated 0.5 M H_2SO_4 or 0.1 M $HClO_4$.

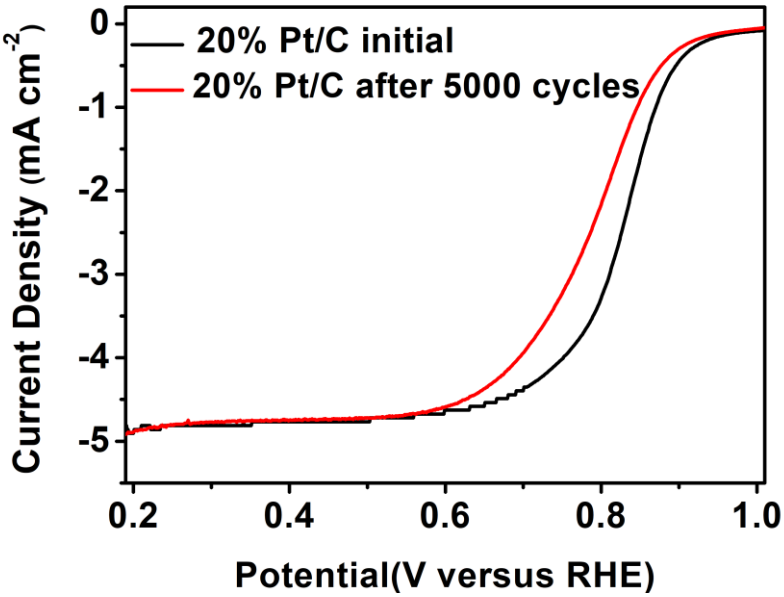

Fig. S16. LSV curves of commercial 20% Pt/C before and after 5000 potential cycles in O_2-saturated 0.1 M $HClO_4$.

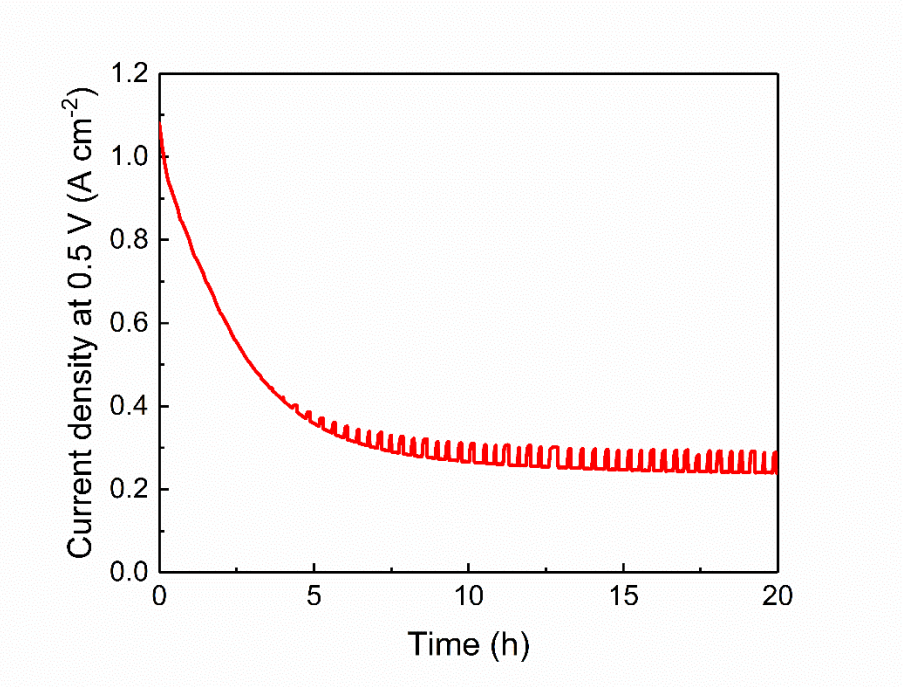

Fig. S17. Single cell stability test of the SA-Fe/NG-based MEA in a PEMFC.

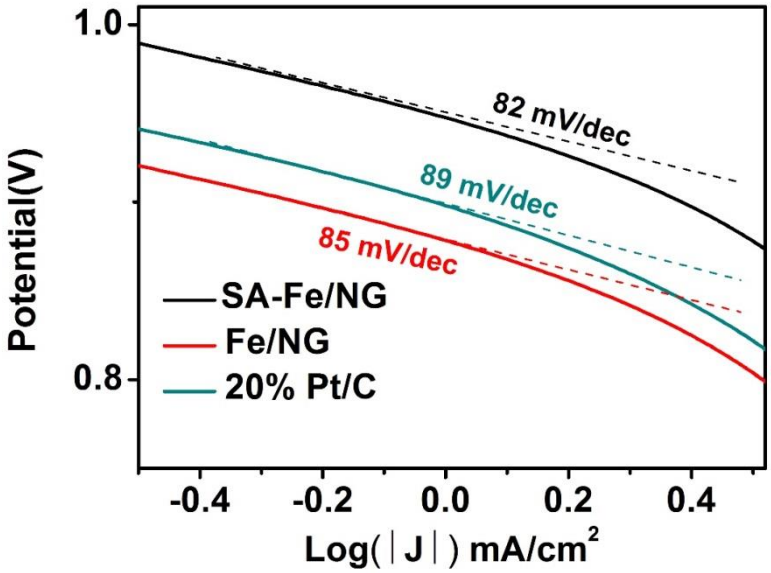

Fig. S18. Tafel plots derived from SA-Fe/NG, Fe/NG and 20% Pt/C in alkaline conditions.

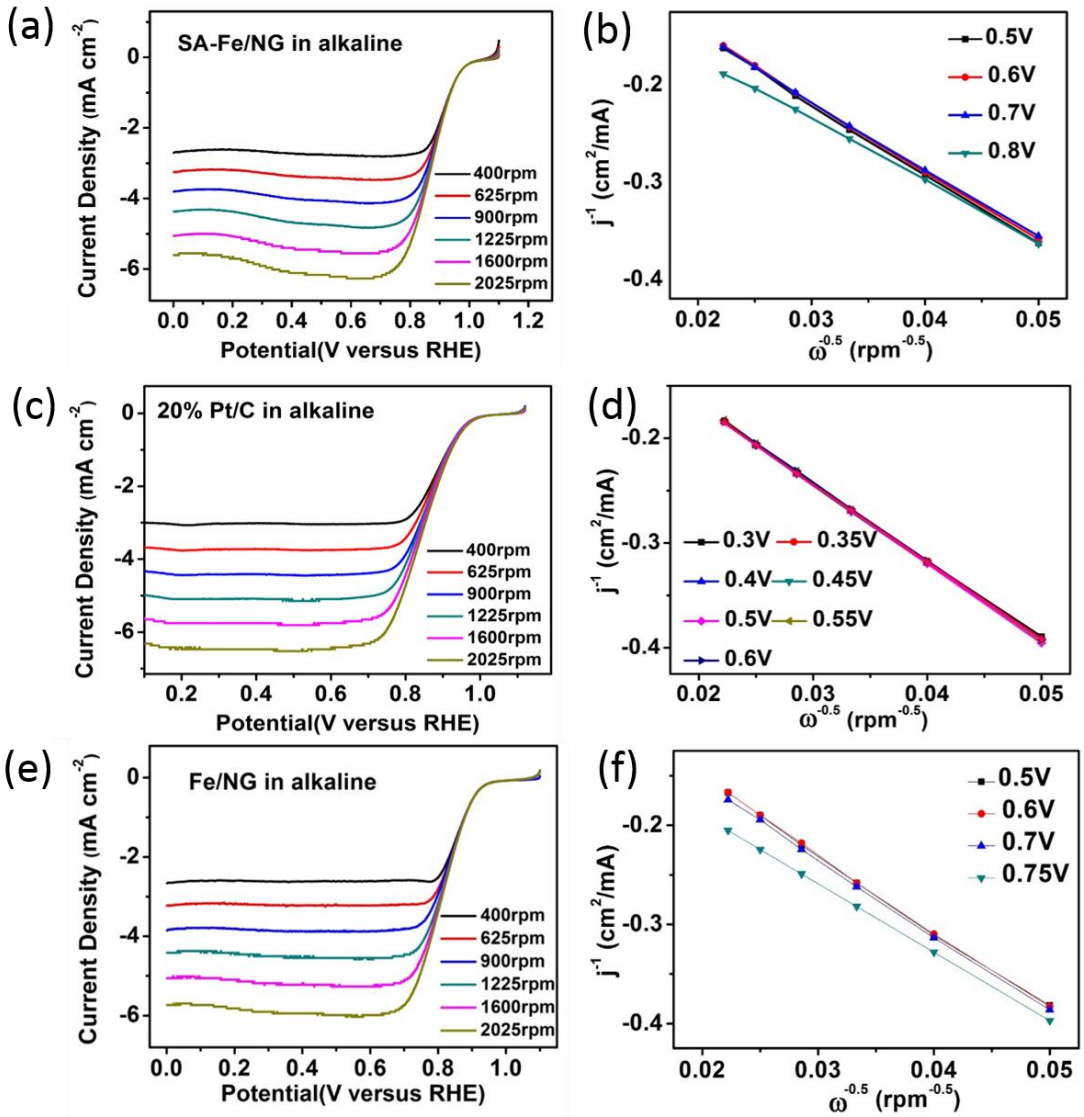

Fig. S19. RDE linear sweep voltammograms of SA-Fe/NG (a), 20% Pt/C (c) and Fe/NG (e) at different rotating speeds in O_2-saturated 0.1M KOH solution with a sweep rate of 5 mV/s at the different rotating rates (400 rpm-2025 rpm). Corresponding Koutecky-Levich plots of SA-Fe/NG (b), 20% Pt/C (d), Fe/NG (f) derived from RDE at different potentials.

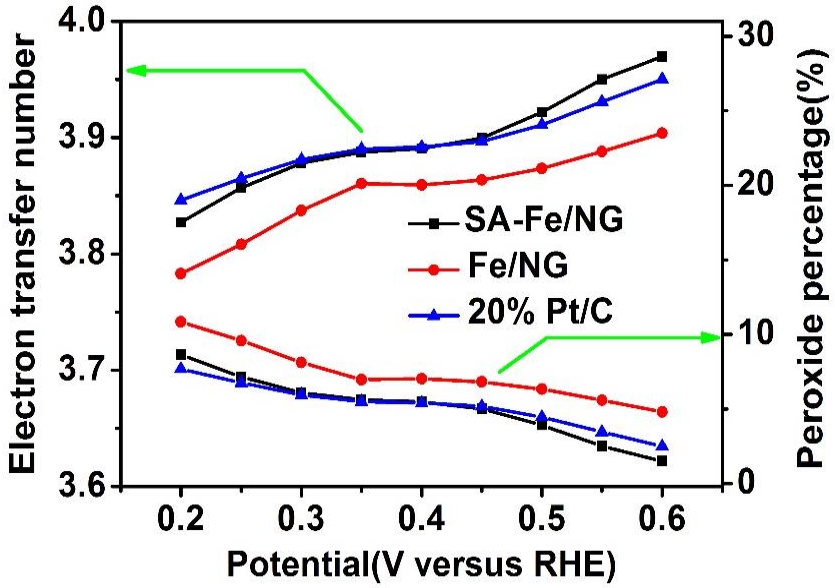

Fig. S20. The percentage proportion of peroxide to the total oxygen reduction products and corresponding electron transfer number n at different potentials (0.2 V-0.6 V) in O_2-saturated 0.1 M KOH.

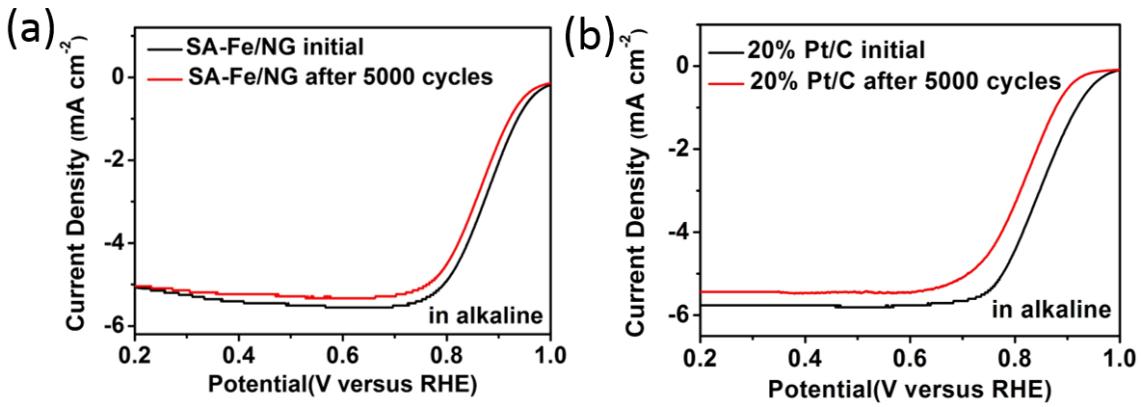

Fig. S21. LSV curves of (a) SA-Fe/NG and (b) 20% Pt/C before and after 5000 potential cycles in O_2-saturated 0.1 M KOH.

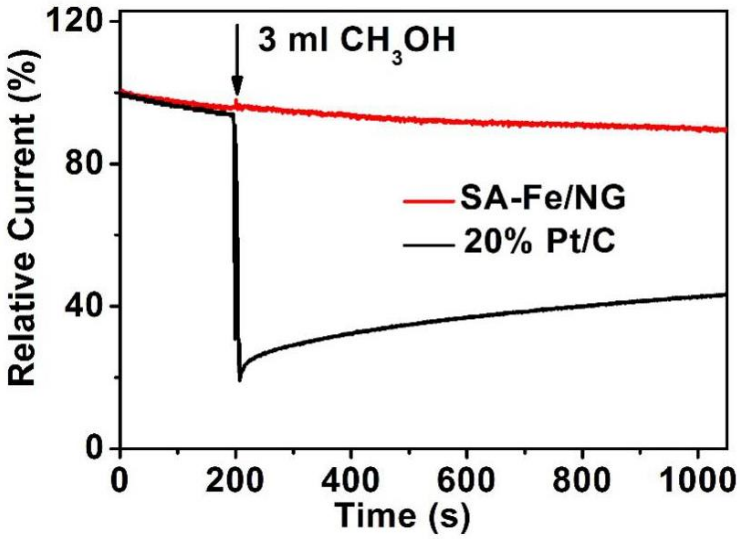

Fig. S22. Methanol resistance of SA-Fe/NG in O_2-saturated 0.1 M KOH without and with CH_3OH.

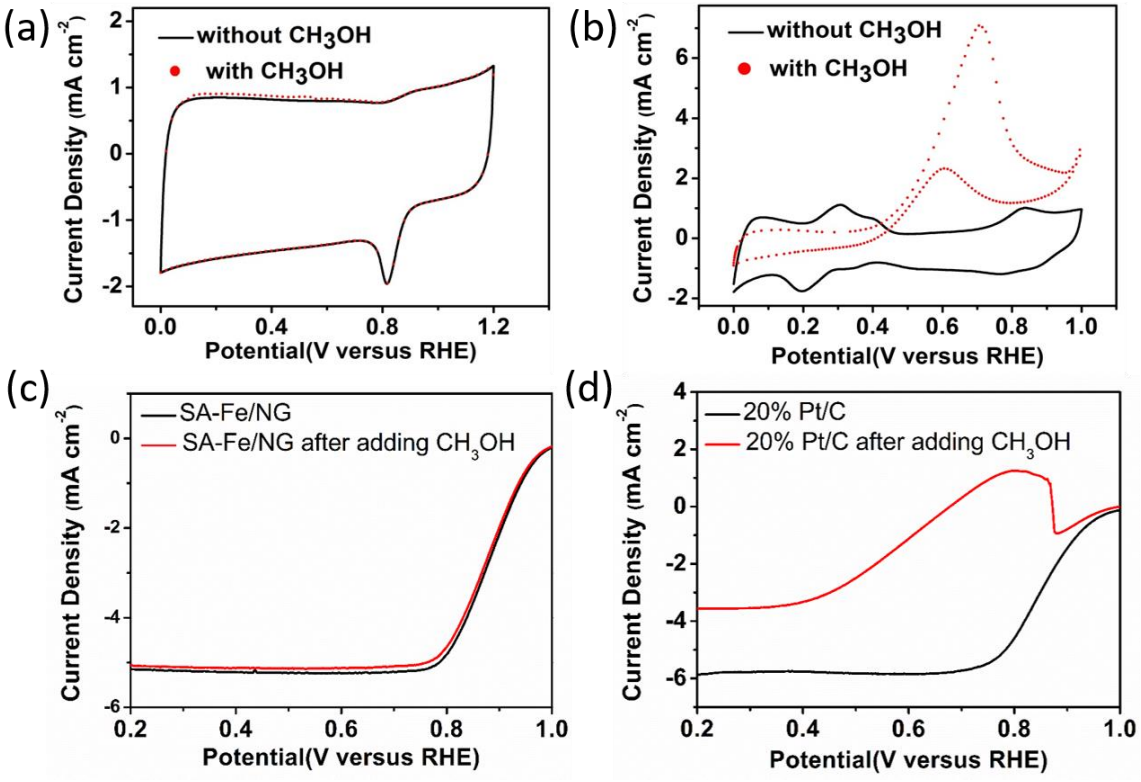

Fig. S23. CV curves of **(a)** SA-Fe/NG catalyst and **(b)** commercial 20% Pt/C in O_2-saturated 0.1 M KOH without and with CH_3OH. LSV curves of **(c)** SA-Fe/NG catalyst and **(d)** commercial 20% Pt/C in O_2-saturated 0.1 M KOH without and with CH_3OH.

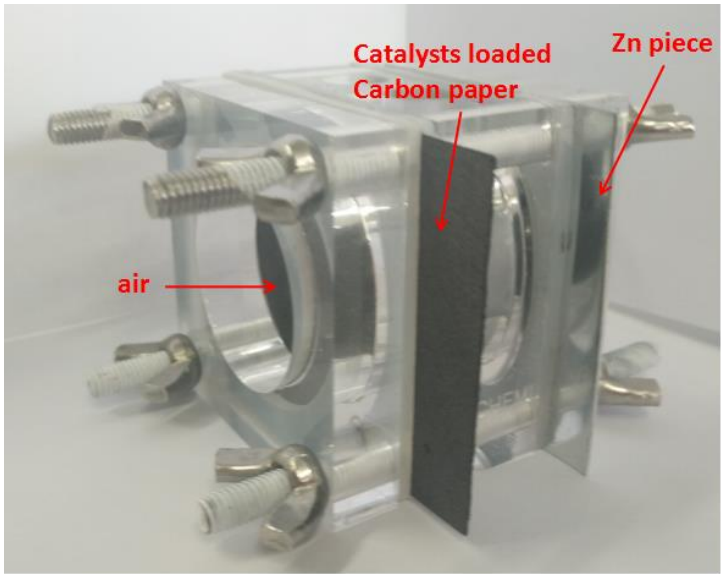

Fig. S24. Photograph of the liquid Zn-air battery.

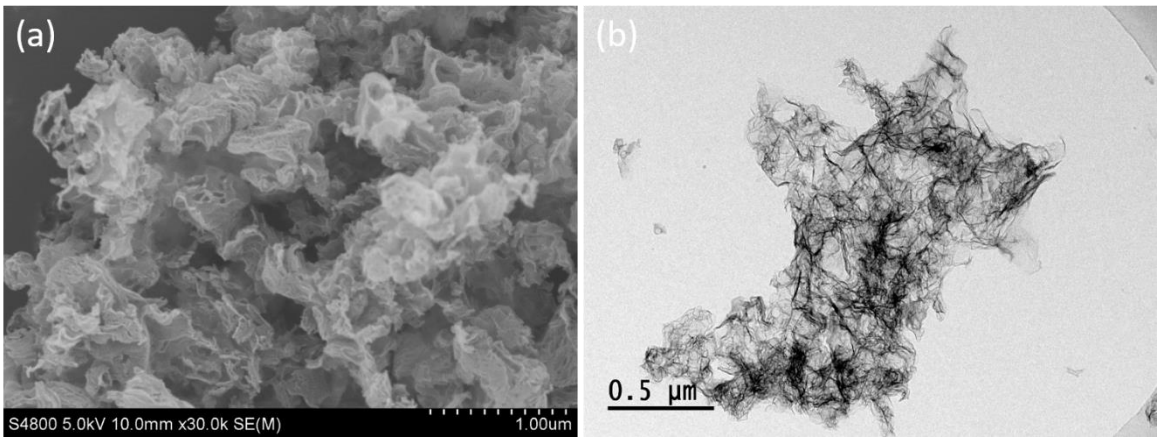

Fig. S25. (a) (b) The SEM and TEM images of SA-Fe/NG catalyst after stability test for Zn-air battery.

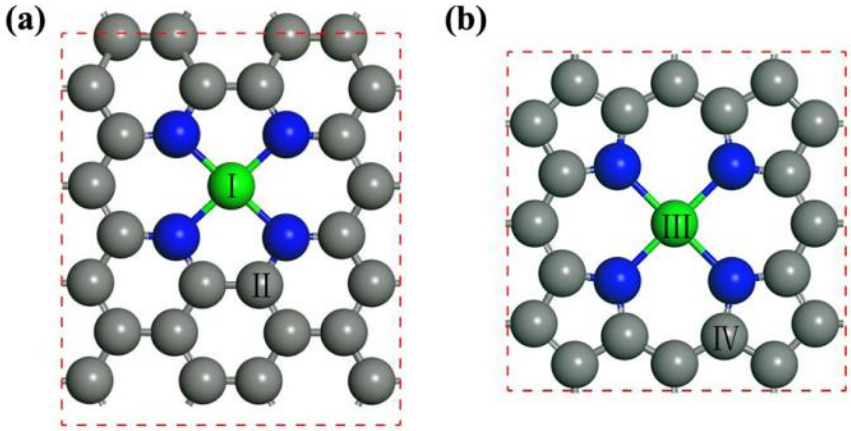

Fig. S26. Repeat cell of computational models of (a) Fe@pyridinic N and (b) Fe@pyrrolic N. The reaction sites considered in this work including Ⅰ: Fe@pyridinic N(Fe), Ⅱ: Fe@pyridinic N(C), Ⅲ: Fe@pyrrolic N(Fe) and Ⅳ: Fe@pyrrolic N(C). The green, blue, and grey balls represent Fe, N, and C atoms, respectively. The unit cells are marked in red dash line.

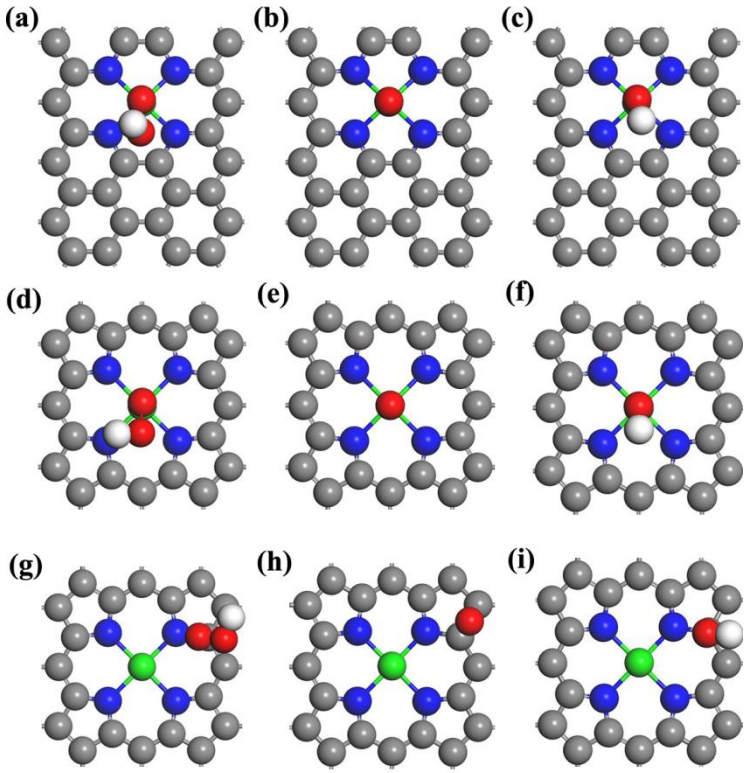

Fig. S27. Configurations of adsorbates (OOH, O and OH) on different catalytic center, including (a-c) Fe@pyridinic N(Fe), (d-f) Fe@pyrrolic N(Fe) and (g-i) Fe@pyrrolic N(C).

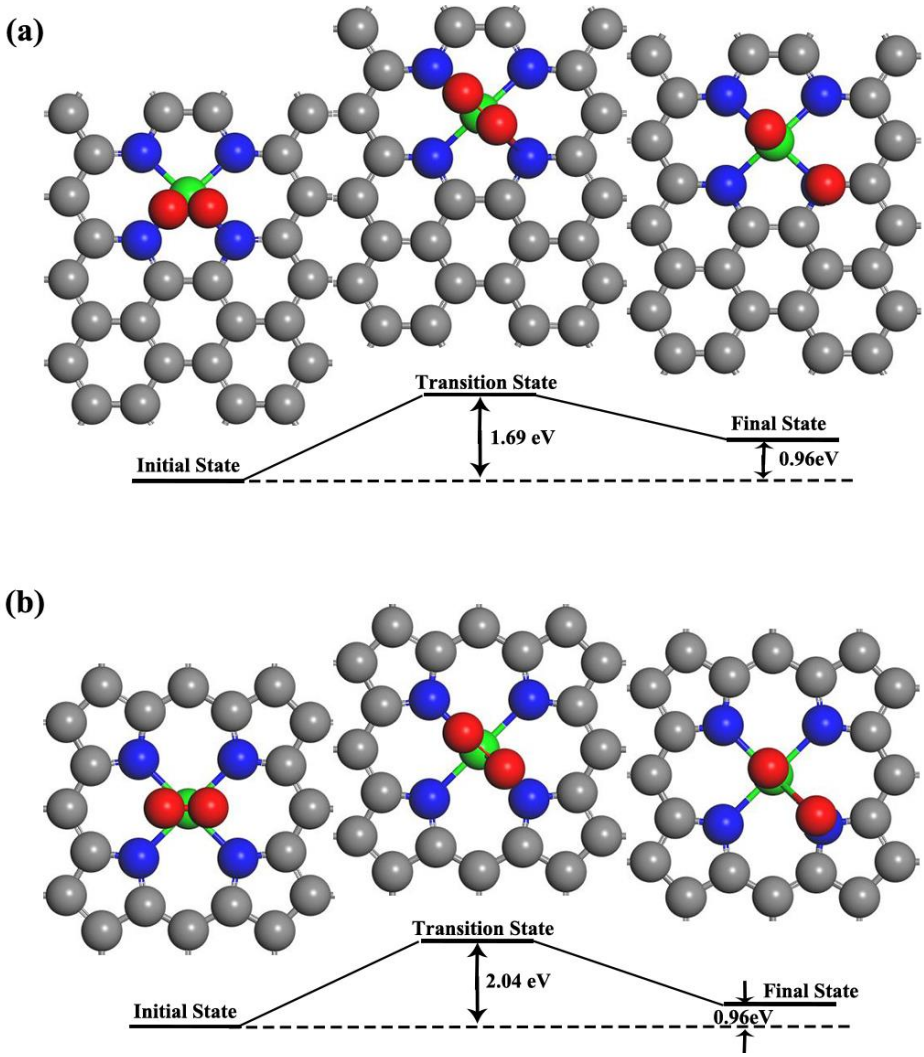

Fig. S28. O_2dissociation pathway on (a) Fe@pyridinic N and (b) Fe@pyrrolic N to form twoadsorbed O*.

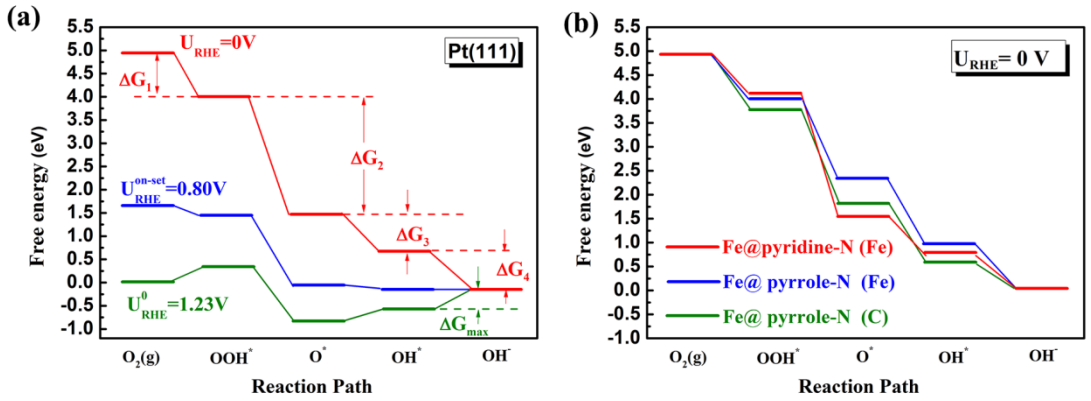

Fig. S29. (a) Free energy diagram for four-electron transferORR on Pt(111) surface at zero electrode potential, on-set electrode potential and equilibrium potential with reversible hydrogen electrode (RHE) in an alkaline electrolyte. (b) Free energy diagram for four-electron transfer ORR on Fe@pyridine-N(Fe), Fe@pyrrole-N(Fe), Fe@pyrrole-N(C) at zero electrode potential with RHE in an alkaline electrolyte.

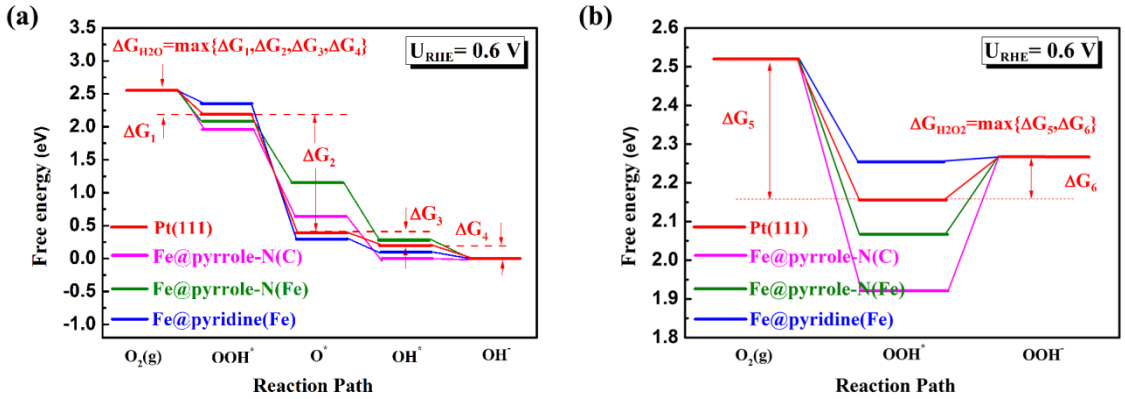

Fig. S30. Free energy diagram for (a) four-electron transfer and (b) two-electron transferORR on Pt(111) surface, Fe@pyridine-N(Fe), Fe@pyrrole-N(Fe) and Fe@pyrrole-N(C) at U_{RHE}=0.6V in an alkaline electrolyte.

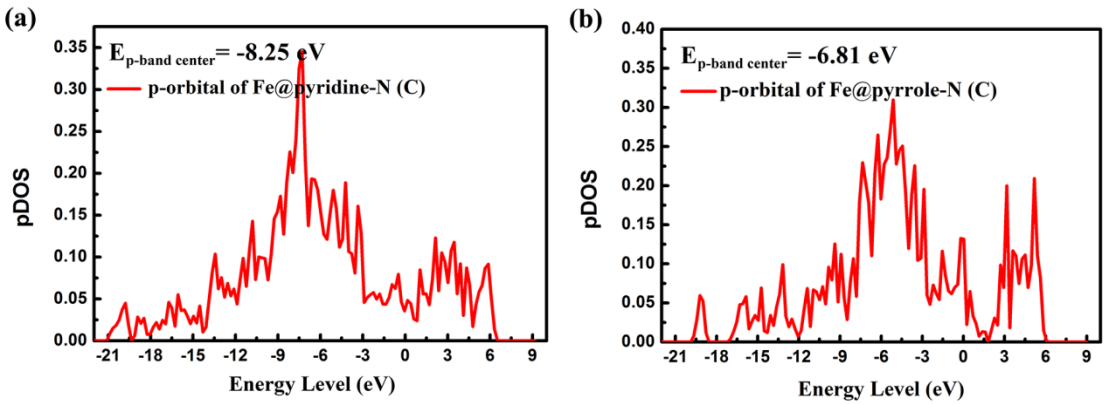

Fig. S31. Projected density of states plots of 2p orbitals for C atom next to N on (a) Fe@pyridinic N and (b) Fe@pyrrolic N.

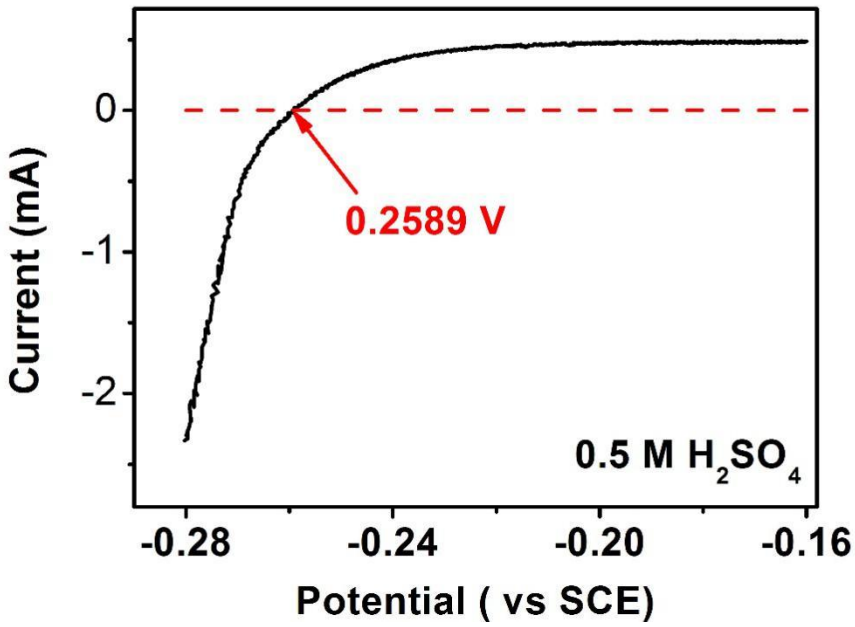

Fig. S32. The calibration of saturated calomel electrode (SCE) as reference electrode with respect to RHE. (In 0.5 M H_2SO_4, $E_{RHE} = E_{SCE} + 0.2589$ V.)

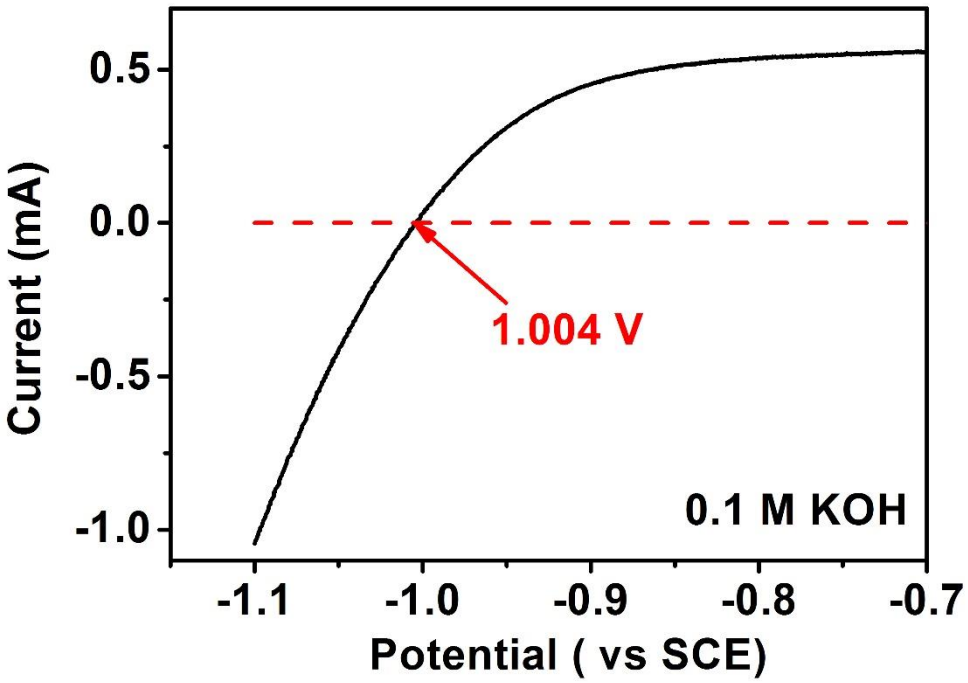

Fig. S33. The calibration of saturated calomel electrode (SCE) as reference electrode with respect to RHE. (In 0.1 M KOH, $E_{RHE} = E_{SCE} + 1.004$ V)

Table S1 Summary of XPS elemental analysis of SA-Fe/NG and Fe/NG

Percentage (at%)	C[at%]	N[at%]	O[at%]	Fe[at%]	pyridinic N [at%]	pyrrolic N/ Fe-N [at%]	graphitic N [at%]
SA-Fe/NG	81.53	11.25	6.63	0.6	31.6	31.9	36.5
Fe/NG	93.62	2.74	3.16	0.48	39.5	11.6	48.8

Table S2 Summary of porosity parameters of SA-Fe/NG, Fe/NG

Samples	S_{BET} ($m^2 g^{-1}$)	$S_{Langumuir}$ ($m^2 g^{-1}$)	Vt ($cm^3 g^{-1}$)	Pore size (nm)	Surface area of micropores (%)	Surface area of mesorpores (%)
SA-Fe/NG	579	1020	1.79	14.4	12.7	87.3
Fe/NG	386	684	0.87	15.5	16.6	83.4

Table S3 Parameters of EXAFS fits for SA-Fe/NG and Fe/NG.

sample	path	Coordination Number	Bond length R （Å）	Bond disorder σ^2 (10^{-3} Å^2)	R factor (%)
SA-Fe/NG	Fe-N	4.0	1.95	3.1	0.457
	Fe-C	3.2	2.6	4.2	
Fe/NG	Fe-N	0.8	1.95	1.8	0.321
	Fe-Fe	7.1	2.6	3.6	
Fe foil	Fe-Fe	8	2.47	3.1	0.227

Table S4 Mössbauer parameters of SA-Fe/NG catalyst derived from the fittings.

Component	IS (mm s^{-1})	QS (mm s^{-1})	LW (mm s^{-1})	Area (%)
D1	0.29	0.97	0.7	23.7
D2	0.4	2.54	1.31	56.1
D3	0.4	1.39	0.58	20.2

Isomer shift (IS), quadrupole splitting (QS), line width (LW) and relative spectral area % of each component.

Table S5 Comparison of the important parameters of non-precious metal catalysts for the ORR in acidic media.

Catalysts	Onset potential (vs RHE)	Half-wave potential (vs RHE)	Limit current (mA cm^{-2})	Ref
SA-Fe/NG	0.9	0.8	5	This work
Fe_3C/C-700	0.9	0.73	4.2	(13)
Fe,N-VACNT	0.97	0.79	6	(14)
Fe-ISAs/CN	0.9	0.79	5.8	(15)
FeCo/C-800	0.9	0.76	5.5	(16)
Fe-CNT-PA	0.6 (Ag/AgCl)	0.42	5.8	(17)
FePhenMOF-NH_3	0.98	0.78	6.4	(18)
PANI-Fe-C	0.98	0.8	3.8	(19)
Fe_3C/NG-800	0.92	0.77	5.8	(20)
FePhen@MOF-NH_3	0.93	0.77	4.8	(21)
$Fe_{0.5}$-950	0.99	0.9	5	(22)
PANI-Fe-C	0.96	0.81	4	(23)
C-Fe-Z8-Ar	0.94	0.82	7.4	(24)
Fe-NrGO-900	0.9	0.79	3.5	(25)
Fe,N-nanoshells	0.85	0.76	5.5	(26)
Fe-N/C	0.86	0.735	5.12	(27)
Cobalt imidazolate	0.83	0.68	4	(28)
Iron imidazolate	0.915	0.76	5	(29)
MDCs	0.82	0.7	5.4	(30)
Fe, Co-NC	0.82	0.72	6	(31)
Fe-N-C	0.99	0.77.	6.2	(32)
Co-N-C	0.85	0.71	5	(33)
Fe-N/C	0.95	0.79	6	(34)
Fe−N/C-800	0.82	0.6	6	(35)
PmPDA-FeNx/C	0.92	0.82	4	(36)

Table S6 Comparison of PEMFC performance of SA-Fe/NG materials with reported state-of-the-art M-N-C catalysts

Catalysts	Conditions	Power density (mW cm^{-2})	Mass loading (mg cm^{-2})	Ref.
FePhen@MOF-Ar NH_3	H_2/Air	380	3	Nat. commun., 2015, 6, 7343
PANI-Fe-MCS		830	4	Nano Energy 2017, 42, 249–256
Fe-N-C-PANI-Phen	H_2/O_2	1060	4	Adv. Mater. 2017, 1604456
ZIF-FA-CNT-p	H_2/O_2	820	4.5	Adv. Mater. 2017, 29, 1604556
Fe-NMCS	H_2/O_2	463	4	Adv. Mater. 2016, 28, 7948–7955
Fe-Z8-C	H_2/O_2	1141	2.8	Angew. Chem. Int. Ed. 2018, 57, 1204–1208
Fe/N/CF	H_2/O_2	900	3	PNAS, 2015, 112, 10631
PFeTPP-1000	H_2/O_2	730	4	Angew. Chem. Int. Ed. 2013, 52, 8349–8353
Fe/PI-1000-III-NH_3	H_2/O_2	600	4	J. Mater. Chem. A, 2014, 2, 11561–11564
FeCBDZ	H_2/O_2	700	4	Adv. Energy Mater. 2014, 4, 1301735
PANI-FeCo-C	H_2/O_2	550	4	Science, 2011, 332, 443-447.
NMCC-C-SiO_2	H_2/O_2	450	2	ElectrochimicaActa 2010, 55, 2853–2858
SA-Fe/NG	H_2/O_2	823	2	This work

Table S7 Values used for the entropy and zero-point energy corrections in determining the free energy of reactants, products, and intermediate species adsorbed on catalysts. For the surface bound species, the ZPE values are averaged over model structures.

Species	T ×S (eV) (298K)	ZPE (eV)
O^*	0	0.07
OH^*	0	0.33
OOH^*	0	0.43
$H_2(g)$	0.41	0.27
$H_2O(g)$	0.58	0.57

Table S8 Adsorption free energies (in eV) of OH, O and OOH on different active sites on catalysts.

Active site	ΔG_{OH}^{*}	ΔG_{O}^{*}	ΔG_{OOH}^{*}
Pt(111)	0.80	1.62	4.00
Fe@pyridinic N(Fe)	0.73	1.52	4.12
Fe@pyrrolic N(Fe)	0.91	2.35	3.93
Fe@pyrrolic N(C)	0.64	1.83	3.75

Table S9 Reaction free energy (in eV vs RHE) of elementary step for four-electron transfer ORR at U_{RHE}=0V, pH=14 on different active sites on catalysts.

Active site	four-electron transfer ORR			
	ΔG_1	ΔG_2	ΔG_3	ΔG_4
Pt(111)	-0.92	-2.38	-0.82	-0.80
Fe@pyridinic N(Fe)	-0.80	-2.60	-0.79	-0.73
Fe@pyrrolic N(Fe)	-0.99	-1.58	-1.44	-0.91
Fe@pyrrolic N(C)	-1.17	-1.92	-1.19	-0.64

Table S10 On-set electron potential ($U^{on\text{-}set}$, in V vs RHE), reaction free energy for potential-determining step at equilibrium potential (ΔG_{max}, in eV) for ORR, reaction free energy of potential-determining step at U_{RHE}=0.6V for four-electron transfer for ORR (ΔG_{H2O2}, in eV), reaction free energy of potential-determining step at U_{RHE}=0.6V for two-electron transfer for ORR (ΔG_{H2O2}, in eV) and difference between ΔG_{H2O} and ΔG_{H2O2} on different active sites on catalysts.

ORR Active site	$U^{on\text{-}set}$	ΔG_{max}	ΔG_{H2O}	ΔG_{H2O2}	ΔG_{H2O}-ΔG_{H2O2}
Pt(111)	0.80	0.43	-0.20	0.13	-0.33
Fe@pyridinic N(Fe)	0.73	0.50	-0.13	0.01	-0.14
Fe@pyrrolic N(Fe)	0.91	0.32	-0.31	0.20	-0.51
Fe@pyrrolic N(C)	0.64	0.59	-0.04	0.38	-0.42

Table S11 Reaction free energy (in eV vs RHE) of elementary step for four-electron transfer and two-electron transfer ORR at U_{RHE}=0.6V, pH=14 on different active sites on catalysts.

Active site	four-electron transfer ORR				two-electron transfer ORR	
	ΔG_1	ΔG_2	ΔG_3	ΔG_4	ΔG_5	ΔG_6
Pt(111)	-0.32	-1.78	-0.22	-0.20	-0.32	0.13
Fe@pyridinic N(Fe)	-0.20	-2.00	-0.19	-0.13	-0.20	0.01
Fe@pyrrolic N(Fe)	-0.39	-0.98	-0.84	-0.31	-0.39	0.20
Fe@pyrrolic N(C)	-0.57	-1.32	-0.59	-0.04	-0.57	0.38

References

1. Kresse G Furthmüller J (1996) Efficiency of ab-initio total energy calculations for metals and semiconductors using a plane-wave basis set. *Comput. Mater. Sci.* 6(1):15-50.
2. Kresse G Furthmüller J (1996) Efficient iterative schemes for ab initio total-energy calculations using a plane-wave basis set. *Phys. Rev. B* 54(54):11169-11186.
3. Perdew J, Burke K, Ernzerhof M (1996) Generalized gradient approximation made simple. *Phys. Rev. Lett.* 77(77):3865-3868.
4. Kresse G Joubert D (1999) From ultrasoft pseudopotentials to the projector augmented-wave method. *Phys. Rev. B* 59:1758-1775.
5. Nørskov J, *et al.* (2004) Origin of the overpotential for oxygen reduction at a fuel-Cell cathode. *J. Phys. Chem. B* 108(46):17886-17892.
6. Jiao Y, Zheng Y, Jaroniec M, Qiao S (2014) Origin of the electrocatalytic oxygen reduction activity of graphene-based catalysts: A roadmap to achieve the best performance. *J. Am. Chem. Soc.* 136(11):4394-4403.
7. Yu L, Pan X, Cao X, Hu P, Bao X (2011) Oxygen reduction reaction mechanism on nitrogen-doped graphene: A density functional theory study. *J. Catal.* 282(1):183-190.
8. Yan H, Xu B, Shi S, Ouyang C (2012) First-principles study of the oxygen adsorption and dissociation on graphene and nitrogen doped graphene for Li-air batteries. *J. Appl. Phys.* 112(10):104316.
9. Desai SK Neurock M (2003) First-principles study of the role of solvent in the dissociation of water over a Pt-Ru alloy. *Phys. Rev. B* 68(7):1071-1086.
10. Rossmeisl J, Qu Z, Zhu H, Kroes G, Nørskov J (2007) Electrolysis of water on oxide surfaces. *J. Electroanal. Chem.* 607(1–2):83-89.
11. Rossmeisl J, Logadottir A, Nørskov JK (2005) Electrolysis of water on (oxidized) metal surfaces. *Chem. Phys.* 319(1–3):178-184.
12. De Paula J (2010) *Atkins' Physical chemistry* (Oxford University Press).
13. Hu Y, *et al.* (2014) Hollow spheres of iron carbide nanoparticles encased in graphitic layers as oxygen reduction catalysts. *Angew. Chem. Int. Ed.* 53(14):3675-3679.
14. Yasuda S, Furuya A, Uchibori Y, Kim J, Murakoshi K (2016) Iron-nitrogen-doped vertically aligned carbon nanotube electrocatalyst for the oxygen reduction reaction. *Adv. Funct. Mater.* 26(5):738-744.
15. Chen Y, *et al.* (2017) Isolated single iron atoms anchored on N-doped porous carbon as an efficient electrocatalyst for the oxygen reduction reaction. *Angew. Chem. Int. Ed.* 129:1-6.
16. Lin Q, *et al.* (2015) Heterometal-embedded organic conjugate frameworks from alternating monomeric iron and cobalt metalloporphyrins and their application in design of porous carbon catalysts. *Adv. Mater.* 27(22):3431-3436.
17. Yang G, Choi W, Pu X, Yu C (2015) Scalable synthesis of bi-functional high-performance carbon nanotube sponge catalysts and electrodes with optimum C-N-Fe coordination for oxygen reduction reaction. *Energy Environ. Sci.* 8(6):1799-1807.
18. Li J, *et al.* (2016) Structural and mechanistic basis for the high activity of iron-nitrogen-carbon electrocatalysts toward oxygen reduction. *Energy Environ. Sci.* 9(7):2418--2432.
19. Wu G, More K, Johnston C, Zelenay P (2011) High-performance electrocatalysts for oxygen reduction derived from polyaniline, iron, and cobalt. *Science* 332(6028):443-447.
20. Xiao M, Zhu J, Feng L, Liu C, Xing W (2015) Meso/macroporous nitrogen-doped carbon architectures with iron carbide encapsulated in graphitic layers as an efficient and robust catalyst for the oxygen reduction reaction in both acidic and alkaline solutions. *Adv. Mater.* 27(15):2521-2527.

21. Strickland K, *et al.* (2015) Highly active oxygen reduction non-platinum group metal electrocatalyst without direct metal–nitrogen coordination. *Nat. Commun.* 6:7343.
22. Zitolo A, *et al.* (2015) Identification of catalytic sites for oxygen reduction in iron- and nitrogen-doped graphene materials. *Nat. Mater.* 14(9):937.
23. Wu G, *et al.* (2011) Synthesis–structure–performance correlation for polyaniline–Me–C non-precious metal cathode catalysts for oxygen reduction in fuel cells. *J. Mater. Chem.* 21(30):11392-11405.
24. Wang X, *et al.* (2016) Directly converting Fe-doped metal–organic frameworks into highly active and stable Fe-N-C catalysts for oxygen reduction in acid. *Nano Energy* 25:110-119.
25. Li Q, *et al.* (2016) High-performance direct methanol fuel cells with precious-metal-free cathode. *Adv. Sci.* 3(11):1600140.
26. Wang Y, Kong A, Chen X, Lin Q, Feng P (2015) Efficient oxygen electroreduction: hierarchical porous Fe–N-doped hollow carbon nanoshells. *ACS Catal.* 5(6):3887-3893.
27. Lai Q, *et al.* (2017) Metal−organic-framework-derived Fe-N/C electrocatalyst with five-coordinated Fe‑Nx sites for advanced oxygen reduction in acid media. *ACS Catal.* 7(7):1655-1663.
28. Ma S, Goenaga GA, Call AV, Liu DJ (2011) Cobalt imidazolate framework as precursor for oxygen reduction reaction electrocatalysts. *Chem. Eur. J.* 17(7):2063–2067.
29. Zhao D, *et al.* (2012) Iron imidazolate framework as precursor for electrocatalysts in polymer electrolyte membrane fuel cells. *Chem. Sci.* 3(11):3200-3205.
30. Xia W, *et al.* (2014) Well-defined carbon polyhedrons prepared from nano metal-organic frameworks for oxygen reduction. *J. Mater. Chem. A* 2(30):11606-11613.
31. Wang X, *et al.* (2016) Noble metal-free oxygen reduction reaction catalysts derived from prussian blue nanocrystals dispersed in polyaniline. *ACS Appl. Mater. Interfaces* 8(13):8436-8444.
32. Liu T, *et al.* (2016) An Fe‑N‑C hybrid electrocatalyst derived from a bimetal‑organic framework for efficient oxygen reduction. *J. Mater. Chem. A* 4(29):11357–11364.
33. Wei J, *et al.* (2015) Nitrogen‑doped nanoporous carbon/graphene nano‑sandwiches: synthesis and application for efficient oxygen reduction. *Adv. Func. Mater.* 25(36):5768-5777.
34. Sa Y, *et al.* (2016) A general approach to preferential formation of active Fe-Nx sites in Fe-N/C electrocatalysts for efficient oxygen reduction reaction. *J. Am. Chem. Soc.* 138(45):15046-15056.
35. Lin L, Zhu Q, Xu AW (2014) Noble-metal-free Fe-N/C catalyst for highly efficient oxygen reduction reaction under both alkaline and acidic conditions. *J. Am. Chem. Soc.* 136(31):11027-11033.
36. Wang Q, *et al.* (2014) Phenylenediamine-based FeN_x/C catalyst with high activity for oxygen reduction in acid medium and its active-site probing. *J. Am. Chem. Soc.* 136(31):10882-10885.